

Boltzmann Thermometry at Cryogenic Temperatures Exploiting Stark Sublevels in $\text{Er}^{3+}/\text{Yb}^{3+}$ -Codoped Yttrium Oxide Nanoparticles

Thomas Possmayer,[†] Allison R. Pessoa,^{*,‡,¶} Jefferson A. O. Galindo,[¶] Luiz F. dos Santos,[§]
Rogéria R. Gonçalves,[§] Anderson M. Amaral,[¶] and Leonardo de S. Menezes^{†,¶}

[†]*Chair in Hybrid Nanosystems, Faculty of Physics, Ludwig-Maximilians-Universität München,
80539 München, Germany*

[‡]*Federal Institute of Education, Science and Technology of Pernambuco, 50740-545 Recife-PE,
Brazil*

[¶]*Department of Physics, Universidade Federal de Pernambuco, 50740-540 Recife-PE, Brazil*

[§]*Department of Chemistry, Center of Nanotechnology and Tissue Engineering- Mater Lumen
Laboratory, Faculty of Philosophy, Science and Letters of Ribeirão Preto, University of São Paulo,
14040-901 Ribeirão Preto-SP, Brazil.*

E-mail: allison.pessoa@ufpe.br

Abstract

The development of reliable luminescent nanothermometers for cryogenic applications is essential for advancing quantum technologies, superconducting systems, and other fields that require precise, high-spatial-resolution temperature monitoring. Lanthanide-doped systems are vastly employed to this purpose, and typically perform optimally at or above room temperature when manifold-to-manifold transitions are used. In this work we exploit individual Stark sublevels to demonstrate an optical thermometer based on $\text{Er}^{3+}/\text{Yb}^{3+}$ codoped yttria (Y_2O_3) nanoparticles that operates effectively across the temperature range from 25 K to 175 K. This is achieved due to the pronounced crystal field environment of the Y_2O_3 host matrix, leading to well-separated Stark lines in the luminescence spectrum of the Er^{3+} ions. By applying the Luminescence Intensity Ratio (LIR) method to transitions originating from two Stark components of the $^4\text{S}_{3/2}$ manifold of the Er^{3+} ions, we achieve thermal sensitivities up to $1.25\% \text{ K}^{-1}$ at 100 K and temperature resolutions reaching 0.2 K. Our results further experimentally confirm recently published theoretical predictions, demonstrating that thermometric performance is not directly dependent on the average (barycenter) difference of the involved electronic energy levels when using individual Stark transitions to evaluate the LIR. The proposed procedure gives an energy gap calibration that matches the one determined by sample spectroscopy for non-overlapping lines in the luminescence spectrum. These insights provide a robust foundation for the design of high-performance cryogenic thermometers based on rare-earth-doped materials.

Keywords

Lanthanide ions; Stark sublevels; Accurate Boltzmann thermometry; Cryogenic optical thermometers

Introduction

The emergence of quantum technologies and the growing demand for precise cryogenic temperature control (at temperature ranges below 140 K) have intensified the need for reliable nanometer- to submicrometer-sized cryothermometers. These

sensors are applicable in areas that go beyond quantum computing,¹ reaching the aerospace industry,² superconductivity-based devices,³ and even medicine and cryobiology.⁴ Lanthanide ion (Ln^{3+})-doped nanoparticles offer a promising platform for nanoscale and non-invasive optical temperature measurements, showing potential to achieve ther-

mal resolutions below 0.1 K.⁵

Luminescence thermometry based on such nanoparticles has been extensively studied, particularly within the biological temperature range (0°C to 50°C).^{6,7} The conventional approach relies on the Luminescence Intensity Ratio (LIR) technique involving two thermally coupled (TC) spin-orbit energy manifolds of the Ln^{3+} ions. This method exploits the Boltzmann distribution governing the electronic population of the ions' energy levels,⁵ which leads to a temperature-dependent emission ratio. Thermometric characteristics such as thermal sensitivity and resolution are directly connected to the energy difference between the TC manifolds.⁵ For instance, Suta & Meijerink showed that the most responsively detected temperature is $T_{\text{opt}} = \Delta E / (2k_{\text{B}})$, where ΔE is the manifold energy separation and k_{B} is Boltzmann's constant.⁸ More recently, Pessoa *et al.* have shown theoretically that this energy separation should be treated as an effective value, ΔE_{eff} , which also incorporates the oscillator strengths of the electronic transitions involved.⁹

For most Ln^{3+} -doped materials, the effective energy difference between spin-orbit manifolds relevant for thermometry is on the order of 10^3 cm^{-1} .^{10,11} Specifically, for Er^{3+} -based sensors, where the $^2\text{H}_{11/2}$ and $^4\text{S}_{3/2}$ manifolds form a TC pair around room temperature, this separation typically ranges from 650 cm^{-1} to 850 cm^{-1} , depending on the host matrix and experimental conditions.⁹ As a result, Boltzmann-type thermometers based on these spin-orbit manifolds operate optimally in the 273 K to 600 K range.⁸

To meet the growing need for cryogenic-range luminescent thermometers, several studies have proposed alternative approaches that exploit the temperature-dependent luminescent behavior of non-TC levels. These include mechanisms such as temperature-dependent non-radiative energy transfer,^{12–14} phonon-assisted energy migration,¹⁵ and variations in luminescence decay time.¹⁶ Only recently, some works have turned toward exploiting individual Stark sublevels within the TC manifolds.^{17–25} These Stark sublevels arise from the splitting of otherwise degenerate spin-orbit levels due to local electric fields in the crystal environment.¹⁰ With typical separations on the order of 10^2 cm^{-1} , they enable optimal thermal responses around 40 K.⁸ However, the applicability of this approach depends strongly on the host matrix, as it must induce sufficiently large and spectrally resolv-

able Stark splittings. Yttria (Y_2O_3) is particularly well-suited for this purpose, as it produces pronounced Stark splitting and narrow emission lines from embedded Ln^{3+} ions.^{26,27}

While optical cryothermometers based on Stark sublevels have been proposed, a comprehensive understanding of the factors governing their sensitivity and accuracy remains unavailable. A recent theoretical framework has exposed and discussed some of these problems.⁹ Specifically, it has been shown that the energy difference between the barycenters of two given Stark lines does not directly determine thermal characteristics, such as the thermometer's relative sensitivity and accuracy, as they do not represent the real relative population distribution and energy difference between the TC Stark sublevels.⁹

In this work, we leverage this insight to choose adequate lines to avoid spectral overlapping and intruding bands - both of which are known to degrade the accuracy of ratiometric thermometry, as already demonstrated for manifold-to-manifold transitions.²⁶ We demonstrate a Boltzmann-type optical thermometer operating in the cryogenic range between 25 K and 175 K based on selected Stark-to-Stark transitions from the Er^{3+} $^4\text{S}_{3/2}$ manifold to the ground state ($^4\text{I}_{15/2}$). Our results validate recently published theoretical predictions⁹ and provide a step forward to achieve accurate and high-precision cryogenic thermometry using rare-earth-doped systems.

Results and Discussions

Upconversion Spectrum at Low Temperatures

In thermometry experiments employing Yb^{3+} / Er^{3+} codoped systems, it is common to excite the TC levels via a two-photon upconversion scheme: Illumination at 980 nm initially populates the $^4\text{F}_{7/2}$ manifold of Er^{3+} ions through a two-step upconversion process assisted by the Yb^{3+} ions in a well-known mechanism of donor-acceptor energy transfer.²⁸ Fig. 1a depicts the unit cell of the used yttria matrix with an Er^{3+} ion substituting an Y^{3+} ion and Fig. 1b shows the relevant photophysical processes under the considered excitation scheme (not showing the Yb^{3+} ions' energy levels for simplicity).

Following the excitation, non-radiative relaxation via electron-phonon interactions transfers population from $^4\text{F}_{7/2}$ to the metastable $^2\text{H}_{11/2}$ and $^4\text{S}_{3/2}$ manifolds. These two levels are considered TC at

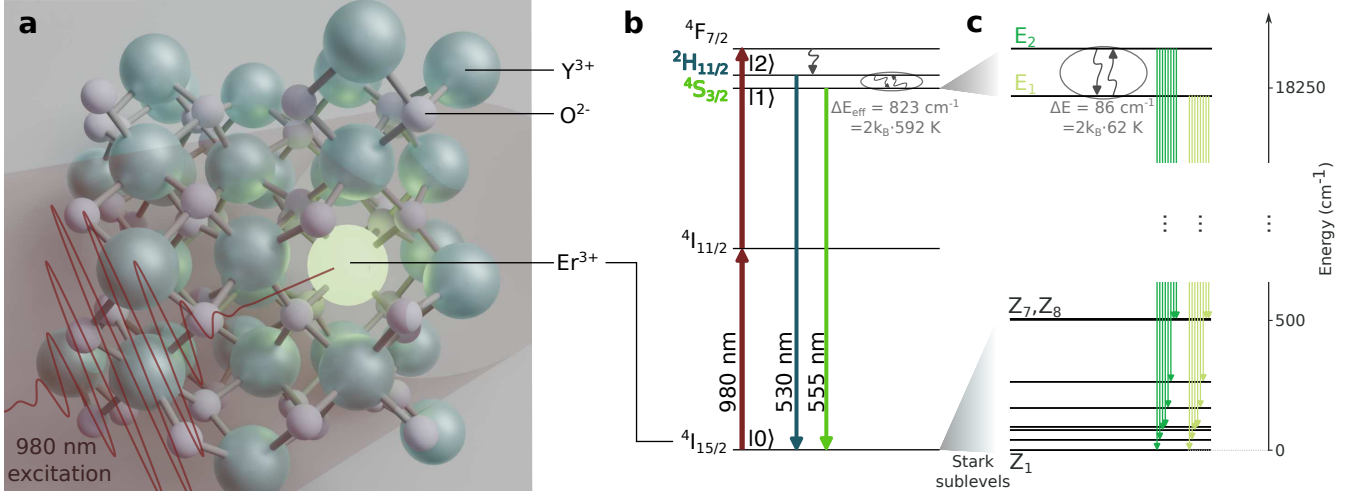


Figure 1: **a**, Unit cell of Y₂O₃ with a doping Er³⁺ ion (bright green) occupying a C_2 symmetry site, emitting upconverted green light under excitation at a wavelength of 980 nm. Turquoise (grey) spheres represent yttrium (oxygen) atoms. **b**, Simplified energy-level diagram of the Er³⁺ ions, showing the relevant levels for nanothermometry via two-photon optical excitation. Upward straight arrows show possible energy transfer mechanisms from Yb³⁺ ions (omitted for clarity) or direct absorption from Er³⁺ ions. Downward straight arrows represent radiative decays; curly arrows indicate non-radiative relaxation processes. Circled levels are considered TC around room temperature and above. **c**, Stark sublevels of the corresponding spin-orbit manifolds. The circled levels are candidates for being used as TC levels in LIR-based optical thermometry experiments performed at cryogenic temperatures.

room temperature, as their energy separation is small enough to allow thermalization in a timescale of nanoseconds to hundreds of nanoseconds, depending on the host matrix,⁹ leading to a population probability distribution well-described by Boltzmann statistics. Both levels subsequently decay radiatively to the ground state (⁴I_{15/2}), emitting photons in the green spectral range. The precise emission wavelengths are determined by the Stark sublevel structure of the excited and ground manifolds (Fig. 1c).

The energy separation and remaining degeneracies of the resulting Stark sublevels are mainly governed by the host matrix. In the Y₂O₃ crystalline material, Er³⁺ and Yb³⁺ ions occupy sites with C_2 and C_{3i} point symmetry, with the optical emission in the green spectral region predominantly stemming from the former site.²⁹ Under this local symmetry, the ²H_{11/2} and ⁴S_{3/2} manifolds split into six and two Stark sublevels, respectively.¹¹ The latter thus provides a potential further pair of TC levels at much lower temperatures (Fig. 1c). Similarly, the ground state ⁴I_{15/2} splits into eight sublevels. Each of these Stark sublevels is a Kramer's doublet and therefore doubly degenerate.¹¹

Assuming that their electronic population follows

Boltzmann statistics, the occupation probability of a Stark sublevel $|i\Gamma_k\rangle$ within the manifold $|i\rangle$ is given by⁹

$$p_{ik}(T) = \frac{g_{ik} \exp\left(-\frac{E_{ik}-E_0}{k_B T}\right)}{\sum_j \sum_{l=1}^{L_j} g_{jl} \exp\left(-\frac{E_{jl}-E_0}{k_B T}\right)}, \quad (1)$$

where g_{jl} is the degeneracy of the Stark sublevel $|j\Gamma_l\rangle$ and E_{jl} is its energy. The reference energy E_0 corresponds to the lowest Stark sublevel of the ⁴S_{3/2} manifold. k_B is Boltzmann's constant and T is the absolute temperature. The sum over j includes both TC manifolds, while the sum over l runs over all L_j Stark sublevels within each manifold.

Temperature variation from cryogenic to room temperature therefore induces significant changes in the electronic population, and consequently also in the emission spectrum (Fig. 2a). These changes arise both from thermal redistribution between the ²H_{11/2} and ⁴S_{3/2} manifolds, and from population changes among their individual Stark sublevels. Fig. 2b shows the measured luminescence spectra at 4.4 K and 305 K, highlighting the higher population probability of the lower-energy manifold at

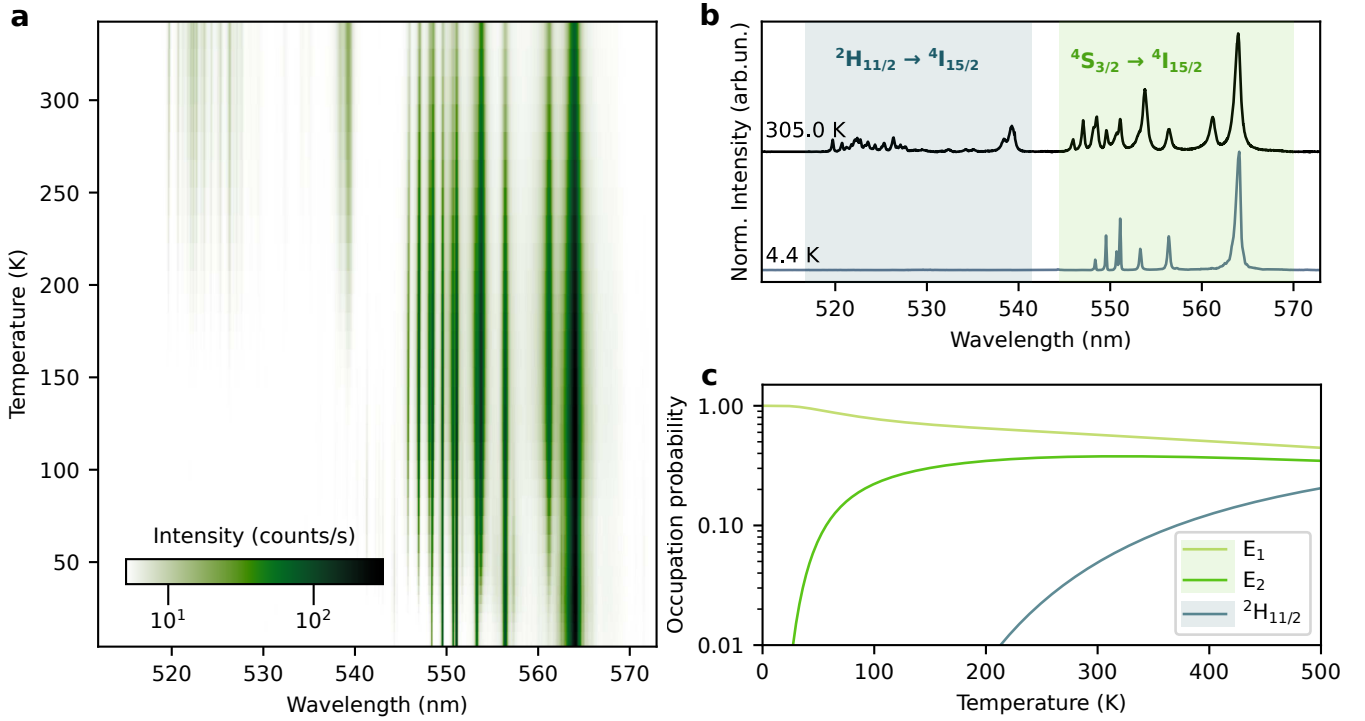


Figure 2: **a**, Temperature-dependent spectra of the upconverted luminescence in the green spectral region emitted by $\text{Y}_2\text{O}_3: \text{Yb}^{3+} / \text{Er}^{3+}$ nanoparticles under 980 nm excitation. Emission from the $^2\text{H}_{11/2}$ manifold is negligible at cryogenic temperatures. **b**, Normalized luminescence spectra at 4.4 K and 305 K (taken from panel **a**) with highlighted manifold transitions. **c**, Calculated occupation probability distribution of the thermally coupled levels of Er^{3+} . Labels E_1 and E_2 correspond to the two Stark components of the $^4\text{S}_{3/2}$ manifold; $^2\text{H}_{11/2}$ denotes the combined population of all Stark sublevels of the $^2\text{H}_{11/2}$ manifold.

low temperatures. The observed spectral lines have average width in the order of 0.8 nm. Emission lines with wavelengths between 517 nm and 542 nm correspond to transitions from Stark sublevels of $^2\text{H}_{11/2}$ to Stark sublevels of the ground state $^4\text{I}_{15/2}$ (respecting possible selection rules), while those between 545 nm and 570 nm correspond to transition between the Stark sublevels of $^4\text{S}_{3/2} \rightarrow ^4\text{I}_{15/2}$.

To further illustrate the temperature-dependent population in the sublevels, Fig. 2c shows calculated occupation probabilities for the two Stark sublevels of the $^4\text{S}_{3/2}$ manifold, labeled as E_1 and E_2 in Fig. 1b (following the empirical notation), as well as the combined occupation probability of all sublevels in the $^2\text{H}_{11/2}$ manifold (labeled as H). These calculations were performed using the levels' energies provided by Kisliuk *et al.*²⁹ for Er^{3+} in a Y_2O_3 matrix. At room temperature, the $^2\text{H}_{11/2}$ manifold becomes appreciably populated, while E_1 and E_2 are close to being equally populated due to their small energy separation. At cryogenic temperatures, however, occupation of the $^2\text{H}_{11/2}$ manifold becomes negligible, and the higher-lying E_2

sublevel is depopulated in favor of E_1 .

Identifying Stark Sublevels

To investigate the population distribution of the TC manifolds by means of the Boltzmann law, we spectroscopically measured the energy separation between their Stark sublevels by analysing the luminescence spectrum. This requires transforming the spectral curve ($I(\lambda)$) to the energy domain, using⁸

$$\tilde{I}(E) = \left(\frac{\lambda^2}{hc} \right) I(\lambda). \quad (2)$$

where h is Planck's constant and c the speed of light in vacuum. Fig. 3 shows the $^4\text{S}_{3/2} \rightarrow ^4\text{I}_{15/2}$ luminescence band converted to the energy scale, along with the assignments of selected Stark-Stark transitions for two different temperatures (a broader temperature sweep is presented in Fig. S1 of the Supporting Information). A similar analysis was performed for the $^2\text{H}_{11/2} \rightarrow ^4\text{I}_{15/2}$ luminescence band at temperatures above 200 K. The extracted ener-

gies of the Stark sublevels - obtained at 140 K for $^4S_{3/2}$ and at 260 K for $^2H_{11/2}$ - are listed in table 1.

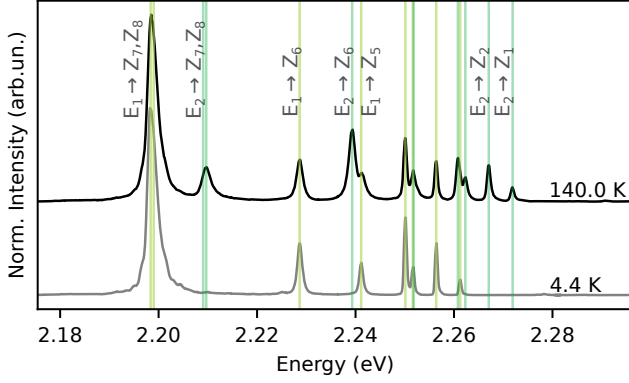


Figure 3: Normalized luminescence spectra of the $^4S_{3/2} \rightarrow ^4I_{15/2}$ band, plotted in energy scale, at 4.4 K and 140 K (offset for clarity). Selected transitions relevant to the thermometric analysis are labeled using empirical notation.

The energy splitting between the two Stark components of the $^4S_{3/2}$ manifold was experimentally determined to be 86 cm^{-1} from the emission spectra. Therefore, at 4.4 K (up to approximately $\sim 20.0 \text{ K}$), nearly all excited ions reside in the lowest Stark sublevel of $^4S_{3/2}$ (E_1), as predicted in Fig. 2c. Accordingly, the luminescence spectrum at this temperature in Fig. 3 exhibits only eight distinct peaks - two of which are spectrally overlapped - corresponding to radiative decays from E_1 to the eight Stark components of the ground state $^4I_{15/2}$ (Z_1 to Z_8).

As the temperature increases and E_2 becomes thermally populated, eight additional spectral lines emerge in the $540 \text{ nm} - 570 \text{ nm}$ range. As shown in Fig. 2a, above 200 K the $^2H_{11/2} \rightarrow ^4I_{15/2}$ emission band also appears, while the intensity of the $^4S_{3/2} \rightarrow ^4I_{15/2}$ transition begins to decrease.

Interestingly, we observed that the overall emission intensity of the $^4S_{3/2} \rightarrow ^4I_{15/2}$ transition reaches a maximum near 140 K (see Fig. S2 of the SI). This behavior is likely attributable to mechanical shifts in the optical illumination or collection paths with varying temperature. Additionally, the number of excited ions depends on the efficiency of the upconversion process, which may itself be temperature dependent due to the thermal activation of energy transfer rates.³⁰ However, as ratiometric thermometry involves comparing emission intensities at the same temperature, such variations do not compromise the accuracy or precision of the

thermometer.

Table 1: Measured energies of the Stark sublevels within the relevant Er^{3+} spin-orbit manifolds in Y_2O_3 at 140 K and 260 K for the $^4S_{3/2}$ and $^2H_{11/2}$ manifold, respectively. Values are compared to literature data from Kisliuk *et al.*²⁹

Spin-orbit manifold	Empirical notation	Energy (cm^{-1}) (this work)	Energy (cm^{-1}) (Ref [29])
$^4I_{15/2}$	Z_1	0	0
	Z_2	39	39
	Z_3	77	76
	Z_4	90	89
	Z_5	162	158
	Z_6	263	258
	Z_7	502	500
	Z_8	507	500
$^4S_{3/2}$	E_1	18238	18231
	E_2	18324	18318
$^2H_{11/2}$	F_1	19041	19038
	F_2	19050	19045
	F_3	19077	19072
	F_4	19192	19187
	F_5	19223	19218
	F_6	19247	19243

Boltzmann Thermometry using Stark Sublevels

For the relative population of two TC levels to be correctly described by a Boltzmann distribution, it is required that the radiative decay rates of the TC levels are much smaller than the non-radiative, phonon-assisted thermalization rate. This condition is satisfied in commonly used host matrices, since the electron-phonon interaction rate leading to thermalization is typically five orders of magnitude greater than the radiative decay rate.³¹ However, photophysical processes such as cross-relaxation, excited-state absorption, or surface quenching - if occurring at rates comparable to that of phonon-mediated relaxation - can disrupt the Boltzmann equilibrium.^{32,33} It is therefore essential to ensure that experimental conditions allow for valid Boltzmann statistics.

The ratiometric Boltzmann method relies on measuring the ratio of integrated intensities of two emission bands originating from thermally coupled manifolds. In standard implementations, the LIR is calculated by integrating the entire manifold-to-manifold emission bands. However, if the host matrix allows for spectral resolution of individ-

ual Stark transitions - as is the case in Y_2O_3 : $\text{Yb}^{3+}/\text{Er}^{3+}$ - then specific Stark-Stark lines can be spectrally isolated and used to compute the LIR and consequently to accurately determine the system's temperature.

The intensity of a spectral line is proportional to the total photon emission rate and can be obtained by integrating the luminescence signal ($I(\lambda)$) over the relevant wavelength range.⁸ Care must be taken to avoid the contribution of accidentally superimposed luminescence bands which are not related to the relevant TC levels, contributing to the calculation of the LIR and leading to inaccuracies in the temperature readout.²⁶ If such intruding bands are identified, they can be separated a posteriori through the use of non-arbitrary methods³⁴ or alternative excitation strategies.³⁵

For a transition from a Stark sublevel $|i\Gamma_k\rangle$ (with $i \in \{^4\text{S}_{3/2}, ^2\text{H}_{11/2}\}$ in our case) to a ground-state sublevel $|^4\text{I}_{15/2}\Gamma_m\rangle \equiv |0\Gamma_m\rangle$, the integrated intensity over a wavelength interval $[\lambda_1, \lambda_2]$ without overlapping spectral lines is proportional to the excited energy level's population n_{ik} via⁹

$$\int_{\lambda_1}^{\lambda_2} I(\lambda) d\lambda = \eta(\tilde{\lambda}_{12}) \Phi_{ik,0m} = \eta(\tilde{\lambda}_{12}) A_{ik,0m} n_{ik} \quad , \quad (3)$$

where $\eta(\tilde{\lambda}_{12})$ is the average detection efficiency across the chosen interval, incorporating system optics and the detector sensitivity. $\Phi_{ik,0m}$ is the photon emission rate in the transition. It is equal to the population in the excited Stark sublevel $|i\Gamma_k\rangle$, n_{ik} , multiplied by the Einstein coefficient for the radiative transition, $A_{ik,0m}$. Similarly, one can obtain the integrated intensity of a complete manifold-to-manifold transition by summing all Stark-Stark contributions.

Pessoa *et al.*⁹ have shown that when employing the LIR method by integrating the complete manifold-to-manifold transitions, the LIR as a function of temperature ($R(T)$) is a weighted sum of exponentials. This can be approximated by a single exponential with effective parameters:

$$R(T)_{\text{manifold}} = \frac{\sum_{km} A_{Hk,0m} g_{Hk} \exp(-E_{Hk}/k_B T)}{\sum_{lm} A_{Sl,0m} g_{Sl} \exp(-E_{Sl}/k_B T)} \approx C_{\text{eff}} \cdot \exp\left(-\frac{\Delta E_{\text{eff}}}{k_B T}\right) \quad , \quad (4)$$

where Hk and Sl label Stark sublevels of the $^2\text{H}_{11/2}$ and $^4\text{S}_{3/2}$ manifolds, respectively. The parameters C_{eff} and ΔE_{eff} can be predicted by expanding Eq. (4) around a central $\beta_c = (k_B T_c)^{-1}$ (where T_c is the central temperature of the range under consideration) and truncating to first order:

$$\ln C_{\text{eff}} = \ln R(T_c) + T_c \cdot S_r(T_c) \quad (5)$$

$$\Delta E_{\text{eff}} = S_r(T_c) \cdot k_B T_c^2 \quad ,$$

where $S_r(T) = \frac{1}{R} \frac{\partial R}{\partial T}$ is the thermometer's relative sensitivity, a common figure of merit for comparing thermometer performances.

In practical applications, C_{eff} and ΔE_{eff} are typically determined through prior calibration, by acquiring a set of emission spectra at externally measured temperatures and fitting $R(T)$ using Eq. (4). However, as shown in Fig. 2, the $^2\text{H}_{11/2}$ manifold is scarcely populated below 200 K (less than 1 % of the total population), rendering manifold-to-manifold thermometry ineffective in the cryogenic regime due to vanishing sensitivities. In contrast, Stark sublevels with energy separations on the order of 100 cm^{-1} can enable Boltzmann thermometry at these lower temperatures. In this case, the LIR for a Stark-to-Stark transition $|i\Gamma_k\rangle$ to $|j\Gamma_l\rangle$ is given by a single exponential function, through⁹

$$R(T)_{\text{Stark}} = \frac{A_{ik,0m} g_{ik}}{A_{jl,0m'} g_{jl}} \cdot \exp\left(-\frac{\Delta E_{ik,jl}}{k_B T}\right) \quad , \quad (6)$$

where it is possible to have $i = j$ and $k \neq l$, which corresponds to using two distinct Stark sublevels from the same manifold. Here, $\Delta E_{ik,jl}$ is simply the actual energy separation between the TC Stark sublevels, assuming perfect Boltzmann thermalization and accurate temperature readout.

This approach allows direct extraction of microscopic quantities from $R(T)_{\text{Stark}}$ through curve fitting. This is not possible for the manifold-to-manifold approach since the expression for ΔE_{eff} (Eq. (5)) involves all oscillator strengths between the Stark sublevels of the TC manifolds

and the ground state. These Stark-Stark oscillator strengths are not straightforward to calculate since 4f-4f transitions are parity-forbidden, making the use of Judd-Ofelt theory necessary, which requires other specific details about the Ln^{3+} -host system.³⁶ Therefore, knowing ΔE_{eff} does not yield direct information about microscopic parameters.

Thermometric Characterization

According to the results presented in Table 1, the Stark sublevels E_1 and E_2 of the $^4\text{S}_{3/2}$ manifold are separated by 86 cm^{-1} , while their radiative decay to the ground state can result in spectral lines separated by more than 590 cm^{-1} due to splitting in the ground-state manifold. To calculate the bands' intensities, we separated the Stark lines by fitting them with Voigt profiles, as shown in Fig. S3 of the SI. Despite their differences in spectral separation, fitting the resulting $R_{\text{Stark}}(T)$ with a Boltzmann factor from Eq. (6) consistently yields $\Delta E_{\text{eff}} = \Delta E_{E_1, E_2} \approx 86\text{ cm}^{-1}$, as spectroscopically determined.

This is illustrated in Fig. 4, using two LIR pairs: i) $E_2 \rightarrow (Z_1 + Z_2)$ vs. $E_1 \rightarrow (Z_7 + Z_8)$, which have a spectral separation of 560.6 cm^{-1} ; and ii) $E_2 \rightarrow (Z_1 + Z_2)$ vs. $E_1 \rightarrow Z_6$, which are separated by 321.3 cm^{-1} (see Fig. 3b for the line assignments). The linear relationship between $\ln(R)$ and $1/T$ confirms that the population can be described by Boltzmann statistics, while the slope yields the effective energy separation, which is statistically equal to 86 cm^{-1} in both cases.

Here it is worth stressing that since the relative sensitivity for Stark-Stark transitions $S_r = \Delta E_{E_1, E_2} / (k_B T^2)$ depends only on the true energy difference between the crystal-field states, it has no relation to the separation between the resulting lines in the spectrum - allowing one to select the most convenient, separable lines.

Another figure of merit characterizing a thermometer is the thermal resolution σ_T , defined as the uncertainty in the temperature measurement. It is calculated via propagation in uncertainties in ΔE_{eff} , C_{eff} and the measured LIR:⁹

$$\sigma_T^2 = \frac{1}{S_r(T_c)^2} \left[\left(\frac{\sigma_\alpha}{T_c} \right)^2 + \sigma_\beta^2 + \left(\frac{\sigma_R}{R} \right)^2 - 2 \frac{\sigma_{\alpha\beta}}{T_c} \right]. \quad (7)$$

where $\alpha = \Delta E_{\text{eff}}/k_B$, $\beta = \ln(C_{\text{eff}})$, and σ_α , σ_β and σ_R are the uncertainties of their corresponding

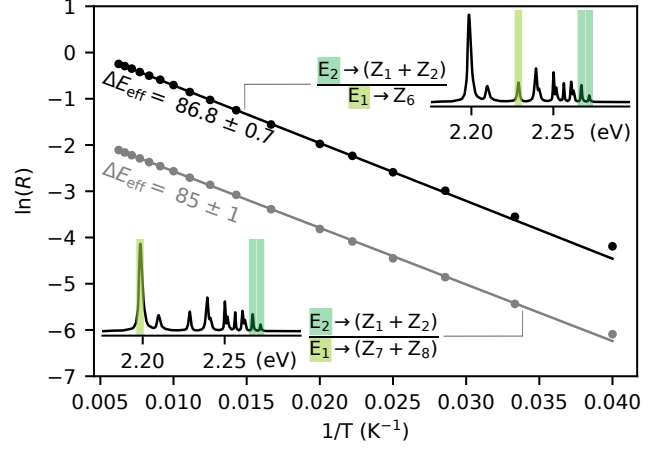


Figure 4: Thermometric characterization using different spectral lines arising from the same thermally coupled Stark sublevels. Insets show spectra from Fig. 3 at 140 K, with the transitions used for the LIR evaluation highlighted.

variables. Note that the uncertainty in determining α and β also depends on the uncertainty of the external thermometer used for calibration of the nanothermometer. $\sigma_{\alpha\beta}$ is the covariance between these two variables, and it was previously shown that it can be a relevant correction.^{37,38} Table 2 presents the full thermometric characterization for selected Stark transitions and compares them to the manifold-based case.

These results confirm that Stark-level thermometry is viable in the 25 K to 175 K range in $\text{Y}_2\text{O}_3:\text{Yb}^{3+}/\text{Er}^{3+}$ systems. For instance, the pair $E_2 \rightarrow (Z_1 + Z_2)$ and $E_1 \rightarrow Z_6$ yields high relative sensitivity in the cryogenic regime (comparable to that of using complete manifolds at room temperature), and yields accurate temperatures. Those lines are well-separated from other lines, thereby reducing artifacts in the temperature measurement related to luminescence band overlapping. In contrast, using $E_2 \rightarrow (Z_1 + Z_2)$ and $E_1 \rightarrow (Z_7 + Z_8)$ introduces partial overlap with $E_2 \rightarrow (Z_7 + Z_8)$, which increases uncertainties at similar sensitivities. Additionally, its lower LIR further increases the thermal uncertainty - consistent with Eq. (7).

The other two investigated pairs ($E_2 \rightarrow (Z_7 + Z_8)$ vs. $E_1 \rightarrow (Z_7 + Z_8)$ and $E_2 \rightarrow Z_6$ vs. $E_1 \rightarrow Z_5$) result in higher sensitivities, but feature spectrally superposed lines, which can compromise the accuracy of the extracted values; in particular, the latter pair has a peak energy separation of just 15 cm^{-1} . It also showed the lowest achieved ther-

Table 2: Thermometric characterization using various spectral lines arising from the same thermally coupled Stark sublevels, including their standard deviations (in parentheses). For completeness, the final row presents the corresponding results using complete manifold-to-manifold integration.

LIR assignment	Temperature range (K)	C_{eff}	ΔE_{eff} (cm^{-1})	ΔE_{bary}^a (cm^{-1})	ΔE_{avg}^a (cm^{-1})	$S_r(T_c)^a$ (% K^{-1})	σ_T^a (K)
$\frac{E_2 \rightarrow (Z_1+Z_2)}{E_1 \rightarrow Z_6}$	25 - 175	1.72(1)	86.8(7)	321.3(1)	86	1.25(1)	0.9
$\frac{E_2 \rightarrow (Z_1+Z_2)}{E_1 \rightarrow (Z_7+Z_8)}$	25 - 175	0.260(4)	85(1)	560.6(1)	86	1.22(2)	1.3
$\frac{E_2 \rightarrow (Z_7+Z_8)}{E_1 \rightarrow (Z_7+Z_8)}$	25 - 175	0.327(2)	64.1(4)	86.7(1)	86	0.922(6)	0.9
$\frac{E_2 \rightarrow Z_6}{E_1 \rightarrow Z_5}$	25 - 175	6.90(1)	70.8(1)	14.9(1)	86	1.018(2)	0.2
Manifold							
$\frac{{}^2\text{H}_{11/2} \rightarrow {}^4\text{I}_{15/2}}{{}^4\text{S}_{3/2} \rightarrow {}^4\text{I}_{13/2}}$	200 - 350	12.4(3)	823(6)	929(1)	859	1.57(1)	1.0

^a At the central temperature of the range, T_c .

mal uncertainty of 0.2 K at $T_c = 100$ K, with $S_r = 1.018\% \text{ K}^{-1}$. This was caused by its higher LIR values, thus improving thermal resolution at the expense of fitting parameters affecting the extracted ΔE_{eff} .

Regarding the manifold-to-manifold characterization, also shown in Table 2, we observe that $\Delta E_{\text{eff}} \neq \Delta E_{\text{bary}} \neq \Delta E_{\text{avg}}$, as theoretically predicted.⁹ Notably, the difference between ΔE_{eff} and ΔE_{bary} exceeds 100 cm^{-1} , implying that the use of ΔE_{bary} instead of ΔE_{eff} in LIR thermometry without careful calibration may lead to temperature errors of more than 35 K at room temperature (295 K). This was estimated by Eq. (7), where we have considered $\sigma_\alpha = 100/k_B$ and $S_r = 1.36$. The other uncertainties were set to zero to analyse only the influence of σ_α in this estimation.

Conclusions

We have demonstrated that an optical nanothermometer based on Y_2O_3 : $\text{Yb}^{3+}/\text{Er}^{3+}$ nanoparticles can operate effectively in the 25 K to 175 K temperature range. The luminescence spectrum of these systems exhibits well-resolved Stark lines with full widths at half maximum around 0.8 nm and minimal spectral overlap. This spectral resolution enables the isolation of individual Stark transitions via Voigt profile fitting. By applying the LIR-based method using the two Stark sublevels of the ${}^4\text{S}_{3/2}$ spin-orbit manifold of the Er^{3+} ions,

we achieved a thermal sensitivity of $1.25\% \text{ K}^{-1}$, and a thermal resolution of 0.2 K. The energy difference between these Stark sublevels is 86 cm^{-1} , measured directly through the luminescence spectra. Although their radiative decays to the Stark-split ground state result in emission lines separated by more than 590 cm^{-1} , we have shown that the thermometer's performance depends solely on the true energy separation of the Stark levels, independent of the energy barycenter of the chosen emission lines. These findings confirm recent theoretical predictions concerning the principles of temperature readout in such systems.⁹

Methods

Sample Synthesis

Nanocrystalline $\text{Er}^{3+} / \text{Yb}^{3+}$ co-doped Y_2O_3 was synthesized through a homogeneous precipitation method followed by controlled thermal treatment to ensure phase purity and crystallinity. Initially, Er^{3+} and Yb^{3+} co-doped yttrium hydroxycarbonate $[\text{Y}(\text{OH})\text{CO}_3 \cdot n\text{H}_2\text{O}]$ was prepared and employed as a precursor. The homogeneous precipitation was achieved through urea thermolysis, conducted in an aqueous solution of yttrium nitrate hexahydrate ($\text{Y}(\text{NO}_3)_3 \cdot 6\text{H}_2\text{O}$, 99.8% purity, Sigma-Aldrich[®]) and urea (99.0% purity, Synth[®]), with final concentrations of 0.01 mol L^{-1} and 5 mol L^{-1} , respectively.

The Er^{3+} and Yb^{3+} dopants were introduced via aqueous solutions of erbium and ytterbium nitrates, which were obtained by dissolving the respective rare-earth oxides (RE_2O_3 , $\text{RE} = \text{Er}, \text{Yb}$) in a slight excess of nitric acid. The acid excess was evaporated until the solution reached a pH of 4, after which the volume was adjusted to achieve a final concentration of 0.1 mol L^{-1} . The dopant concentrations of Er^{3+} and Yb^{3+} were fixed at 0.5 mol% and 1.5 mol%, respectively, relative to the molar concentration of Y^{3+} .

The thermolysis reaction was conducted in a sealed vessel at 80°C for 2 hours, allowing for the precipitation of the co-doped precursor nanoparticles. The resulting precipitate was separated by centrifugation at 4000 rpm, washed five times with distilled water, and subsequently dried at 70°C for 6 hours. The final Er^{3+} , Yb^{3+} co-doped Y_2O_3 nanoparticles were obtained by annealing the $\text{Y}(\text{OH})\text{CO}_3 \cdot n\text{H}_2\text{O}$ precursor in air at 900°C for 2 hours, using a controlled heating rate of 5°C min^{-1} . X-ray diffraction (XRD) and Transmission Electron Microscopy (TEM) data are shown in Figs. S4a and S4b of the Supporting Information, respectively. The resulting particles had an average diameter of $80 \pm 10 \text{ nm}$.

Experimental Setup

The dry nanoparticle powder was compacted into a copper sample holder and placed inside a closed-cycle cryostat (Cryostation[®] s50 - Montana Instruments), capable of controlling the sample temperature between 4.4 K and 350 K. The cryostat reference temperature has an accuracy of 5 mK at 4.4 K and 65 mK at 350 K, according to the manufacturer.

Excitation was performed using a femtosecond laser source (Chameleon[®] Ultra II - Coherent) operating at 980 nm with an 80 MHz repetition rate and a spectral width of approximately 10 nm. A 35 mm focal length lens was placed inside the cryostat for both excitation and collection of the luminescence signal in reflection geometry (see supplementary Fig. S5). The excitation beam had a Gaussian profile, with an estimated focal volume of $2 \times 10^{-11} \text{ cm}^3$.

A beam splitter was used to separate the emission from the excitation light. The collected luminescence was directed into a spectrometer (Acton SP2300 - Princeton Instruments), coupled to a CCD camera (Pixis 100F - Princeton Instru-

ments). A 1800 grooves/mm diffraction grating enabled spectral resolution of individual Stark lines. The integration time for all spectra was 60 s.

Acknowledgement L. de S. Menezes and T. Possmayer acknowledge the support from the Center for Nanoscience (CeNS), Ludwig Maximilians-Universität München, Germany, and the Bavarian program Enabling Quantum Communication and Imaging Applications (EQAP). L. F. dos Santos acknowledges FAPESP (grant numbers: 2020/04157-5 and 2023/03092-5). R. R. Gonçalves acknowledges CNPq (grant number 303110/2019-8 and 306191/2023-7), FAPESP (grant number 2020/05319-9 and 2017/11301-2) and INCT-INFo for financial support. A. M. Amaral and A. R. Pessoa acknowledge the financial support by CAPES and INCT-INFo.

Supporting Information Available

Supporting information provides details on sample's characterization and Stark sublevels separation through Voigt profile fitting.

CRedit author statement: T. POSS-MAYER: Investigation, Formal analysis, Writing-Original draft; A. R. PESSOA: Conceptualization, Formal analysis, Writing- Original draft; J. A. O. GALINDO: Formal analysis, Writing- review & editing; L. F. dos SANTOS: Resources, Writing-Original draft; R. R. GONÇALVES: Resources, Writing- review & editing; A. M. AMARAL: Supervision, Project Administration, Writing- review & editing; L. de S. MENEZES: Supervision, Project Administration, Writing- review & editing.

References

- (1) Brandl, M. F.; van Mourik, M. W.; Postler, L.; Nolf, A.; Lakhmanskiy, K.; Paiva, R. R.; Möller, S.; Daniilidis, N.; Häffner, H.; Kaushal, V. *et al.* Cryogenic setup for trapped ion quantum computing. *Review of Scientific Instruments* **2016**, *87*, 113103.
- (2) Kale, A.; Khanna, N. A Review on Cryogenic Machining of Super Alloys Used in Aerospace Industry. *Procedia Manufacturing* **2017**, *7*, 191–197.
- (3) Van Sciver, S. W. Cryogenic systems for superconducting devices. *Physica C: Superconductivity* **2001**, *354*, 129–135.
- (4) Jain, P.; Agarwal, P.; Mathur, D.; Singh, P.; Sharma, A. Evolution of cryogenics – A review on applications of cryogenics in medicine. *Materials Today: Proceedings* **2021**, *47*, 3059–3063.
- (5) Brites, C.; Millán, A.; Carlos, L. In *Including Actinides*; Jean-Claude, B., Vitalij K., P., Eds.; Handbook on the Physics and Chemistry of Rare Earths; Elsevier, 2016; Vol. 49; pp 339–427.
- (6) Bednarkiewicz, A.; Drabik, J.; Trejgis, K.; Jaque, D.; Ximendes, E.; Marciniak, L. Luminescence based temperature bio-imaging: Status, challenges, and perspectives. *Applied Physics Reviews* **2021**, *8*, 011317.
- (7) Gonçalves, I. M.; Pessoa, A. R.; Hazra, C.; Correales, Y. S.; Ribeiro, S. J. L.; de S. Menezes, L. Phonon-assisted NIR-to-visible upconversion in single β -NaYF₄ microcrystals codoped with Er³⁺ and Yb³⁺ for microthermometry applications: Experiment and theory. *Journal of Luminescence* **2021**, *231*, 117801.
- (8) Suta, M.; Meijerink, A. A Theoretical Framework for Ratiometric Single Ion Luminescent Thermometers—Thermodynamic and Kinetic Guidelines for Optimized Performance. *Advanced Theory and Simulations* **2020**, *3*, 2000176.
- (9) Pessoa, A. R.; de S. Menezes, L.; Amaral, A. M. Addressing Discrepancies between Theory and Experiments in Boltzmann Luminescence Thermometry with Ln³⁺ Ions. *The Journal of Physical Chemistry C* **2025**, *129*, 11143–11154.
- (10) Malta, O. L.; Carlos, L. D. Intensities of 4f-4f transitions in glass materials. *Química Nova* **2003**, *26*, 889–895.
- (11) Bünzli, J.-C. G.; Eliseeva, S. V. In *Lanthanide Luminescence*; Hänninen, P., Härmä, H., Eds.; Springer Berlin Heidelberg: Berlin, Heidelberg, 2010; Vol. 7; pp 1–45, Series Title: Springer Series on Fluorescence.
- (12) Wei, H.; Cai, Z.; Huang, H.; Wei, G.; Zhou, B. Ultra-Sensitive Low-Temperature Upconversion via Interfacial Energy Transfer Toward Visual Cryogenic Nanothermometry. *Advanced Functional Materials* *n/a*, e10764.
- (13) Ren, M.; Brites, C. D. S.; Bao, S.-S.; Ferreira, R. A. S.; Zheng, L.-M.; Carlos, L. D. A cryogenic luminescent ratiometric thermometer based on a lanthanide phosphonate dimer. *J. Mater. Chem. C* **2015**, *3*, 8480–8484.
- (14) N’Dala-Louika, I.; Ananias, D.; Latouche, C.; Dessapt, R.; Carlos, L. D.; Serier-Brault, H. Ratiometric mixed Eu–Tb metal–organic framework as a new cryogenic luminescent thermometer. *J. Mater. Chem. C* **2017**, *5*, 10933–10937.
- (15) Liu, X.; Akerboom, S.; Jong, M. d.; Mutikainen, I.; Tanase, S.; Meijerink, A.; Bouwman, E. Mixed-Lanthanoid Metal–Organic Framework for Ratiometric Cryogenic Temperature Sensing. *Inorganic Chemistry* **2015**, *54*, 11323–11329.

- (16) Bolek, P.; Zeler, J.; Brites, C. D.; Trojan-Piegza, J.; Carlos, L. D.; Zych, E. Ga-modified YAG:Pr³⁺ dual-mode tunable luminescence thermometers. *Chemical Engineering Journal* **2021**, *421*, 129764.
- (17) Sukul, P. P.; Singh, Y.; Swart, H. Ultra-wide band near-infrared (NIR) optical thermometry (12–673 K) performance enhanced by Stark sublevel splitting in Er³⁺ ions near the first biological window in the PbZr_{0.53}Ti_{0.47}O₃:Er³⁺/Yb³⁺ phosphor. *Phys. Chem. Chem. Phys.* **2025**, *27*, 270–282.
- (18) Li, Y.; Jiang, S.; Zhong, L.; Wang, Y.; Yang, B.; Wang, Y.; Xiang, G.; Tang, X.; Ling, F.; Li, L. *et al.* Ultra-sensitive low-temperature luminescent thermometry based on Boltzmann behavior of the Stark sub-levels of Pr³⁺. *Journal of Alloys and Compounds* **2024**, *1009*, 176842.
- (19) Dodson, A.; Wu, H.; Rai, A.; Apte, S.; O’Hara, A.; Lawrie, B.; Wang, Y.; Ueda, A.; Krzyżanowska, H.; Titze, M. *et al.* Phonon-mediated temperature dependence of Er³⁺ optical transitions in Er₂O₃. *Communications Physics* **2024**, *7*.
- (20) Boldyrev, K. N.; Diab, M.; Khaidukov, N. M.; Popova, M. N. Luminescent Cryothermometer Based on K₂YF₅:Er³⁺. *Optics and Spectroscopy* **2024**, *132*, 216–222.
- (21) Zhang, L.; Wu, J.; Cui, Y.; Sun, H.; Ning, C.-Z. Self-optimized single-nanowire photoluminescence thermometry. *Light: Science & Applications* **2023**, *12*, 36.
- (22) Kalinichev, A. A.; Afanaseva, E. V.; Kolesnikov, E. Y.; Kolesnikov, I. E. Boltzmann-type cryogenic radiometric thermometry based on Nd³⁺-doped LuVO₄ phosphors. *J. Mater. Chem. C* **2023**, *11*, 12234–12242.
- (23) Kitos, A. A.; Gállico, D. A.; Castañeda, R.; Ovens, J. S.; Murugesu, M.; Brusso, J. L. Stark Sublevel-Based Thermometry with Tb(III) and Dy(III) Complexes Cosensitized via the 2-Amidinopyridine Ligand. *Inorganic Chemistry* **2020**, *59*, 11061–11070.
- (24) Shang, Y.; Han, Q.; Hao, S.; Chen, T.; Zhu, Y.; Wang, Z.; Yang, C. Dual-Mode Upconversion Nanoprobe Enables Broad-Range Thermometry from Cryogenic to Room Temperature. *ACS Applied Materials & Interfaces* **2019**, *11*, 42455–42461.
- (25) Yu, D.; Li, H.; Zhang, D.; Zhang, Q.; Meijerink, A.; Suta, M. One ion to catch them all: Targeted high-precision Boltzmann thermometry over a wide temperature range with Gd³⁺. *Light: Science & Applications* **2021**, *10*, 236.
- (26) Pessoa, A. R.; Galindo, J. A. O.; dos Santos, L. F.; Gonçalves, R. R.; Maier, S. A.; de S. Menezes, L.; Amaral, A. M. Correction Due to Nonthermally Coupled Emission Bands and Its Implications on the Performance of Y₂O₃: Yb³⁺/Er³⁺ Single-Particle Thermometers. *The Journal of Physical Chemistry C* **2023**, *127*, 9673–9680.
- (27) Casabone, B.; Benedikter, J.; Hümmer, T.; Oehl, F.; de Oliveira Lima, K.; Hänsch, T. W.; Ferrier, A.; Goldner, P.; de Riedmatten, H.; Hunger, D. Cavity-enhanced spectroscopy of a few-ion ensemble in Eu³⁺:Y₂O₃. *New Journal of Physics* **2018**, *20*, 095006.
- (28) Hinojosa, S.; Meneses-Nava, M.; Barbosa-García, O.; Díaz-Torres, L.; Santoyo, M.; Mosiño, J. Energy back transfer, migration and energy transfer (Yb-to-Er and Er-to-Yb) processes in Yb,Er:YAG. *Journal of Luminescence* **2003**, *102-103*, 694–698.
- (29) Kisliuk, P.; Krupke, W. F.; Gruber, J. B. Spectrum of Er³⁺ in Single Crystals of Y₂O₃. *The Journal of Chemical Physics* **1964**, *40*, 3606–3610.
- (30) Yu, W.; Xu, W.; Song, H.; Zhang, S. Temperature-dependent upconversion luminescence and dynamics of NaYF₄:Yb³⁺/Er³⁺ nanocrystals: influence of particle size and crystalline phase. *Dalton Trans.* **2014**, *43*, 6139–6147.

- (31) Yu, D.; Ballato, J.; Riman, R. E. Temperature-Dependence of Multiphonon Relaxation of Rare-Earth Ions in Solid-State Hosts. *The Journal of Physical Chemistry C* **2016**, *120*, 9958–9964.
- (32) Suta, M.; Antić, Ž.; Đorđević, V.; Kuzman, S.; Dramićanin, M. D.; Meijerink, A. Making Nd^{3+} a Sensitive Luminescent Thermometer for Physiological Temperatures—An Account of Pitfalls in Boltzmann Thermometry. *Nanomaterials* **2020**, *10*, 543.
- (33) Galvão, R.; dos Santos, L. F.; de O. Lima, K.; Gonçalves, R. R.; de S. Menezes, L. Single $\text{Yb}^{3+}/\text{Er}^{3+}$ -Codoped Yttria Nanocrystals for Temperature Sensing: Experimental Characterization and Theoretical Modeling. *The Journal of Physical Chemistry C* **2021**, *125*, 14807–14817.
- (34) Galindo, J. A.; Pessoa, A. R.; Serge-Correales, Y. E.; Ribeiro, S. J.; de S. Menezes, L.; Amaral, A. M. Method for separating spectrally overlapping multiphoton upconverted emission bands through spectral power dependence analysis. *Journal of Luminescence* **2023**, *257*, 119685.
- (35) Pessoa, A. R.; Galindo, J. A.; Possmayer, T.; Amaral, A. M.; Verelst, M.; Maier, S. A.; de S. Menezes, L. Luminescence thermometry with $\text{Gd}_2\text{O}_2\text{S}:\text{Yb}^{3+}/\text{Er}^{3+}$ nanoparticles under different excitation pathways. *Optical Materials* **2024**, *153*, 115574.
- (36) Walsh, B. M. Judd-Ofelt theory: principles and practices. *Advances in Spectroscopy for Lasers and Sensing*. Dordrecht, 2006; pp 403–433.
- (37) Galindo, J. A. O.; Pessoa, A. R.; Amaral, A. M.; de S. Menezes, L. Influence of the surrounding medium on the luminescence-based thermometric properties of single $\text{Yb}^{3+}/\text{Er}^{3+}$ codoped yttria nanocrystals. *Nanoscale Adv.* **2021**, *3*, 6231–6241.
- (38) Galindo, J. A. O.; Pessoa, A. R.; Amaral, A. M.; dos Santos, L. F.; Gonçalves, R. R.; de S. Menezes, L. Correction: Influence of the surrounding medium on the luminescence-based thermometric properties of single $\text{Yb}^{3+}/\text{Er}^{3+}$ codoped yttria nanocrystals. *Nanoscale Adv.* **2021**, *3*, 7007–7007.

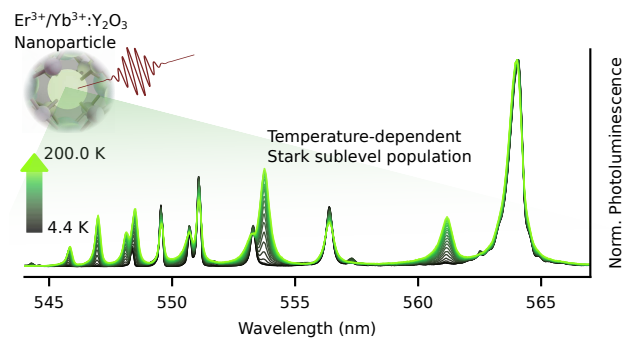


Figure 5: TOC Graphic

Supporting Information:

Boltzmann Thermometry at Cryogenic Temperatures

Exploiting Stark Sublevels in $\text{Er}^{3+}/\text{Yb}^{3+}$ -Codoped Yttrium Oxide Nanoparticles

Thomas Possmayer,[†] Allison R. Pessoa,^{*,‡,¶} Jefferson A. O. Galindo,[¶] Luiz F. dos Santos,[§]
Rogéria R. Gonçalves,[§] Anderson M. Amaral,[¶] and Leonardo de S. Menezes^{†,¶}

[†]*Chair in Hybrid Nanosystems, Faculty of Physics, Ludwig-Maximilians-Universität München,
80539 München, Germany*

[‡]*Federal Institute of Education, Science and Technology of Pernambuco, 50740-545 Recife-PE,
Brazil*

[¶]*Department of Physics, Universidade Federal de Pernambuco, 50740-540 Recife-PE, Brazil*

[§]*Department of Chemistry, Center of Nanotechnology and Tissue Engineering- Mater Lumen
Laboratory, Faculty of Philosophy, Science and Letters of Ribeirão Preto, University of São Paulo,
14040-901 Ribeirão Preto-SP, Brazil.*

E-mail: allison.pessoa@ufpe.br

Contents

S1 Stark-resolved spectra	S-2
S2 Integrated intensity	S-3
S3 Voigt profile fitting	S-3
S4 Sample characterization	S-4
S5 Experimental setup	S-5
References	S-6

S1 Stark-resolved spectra

The $^4S_{3/2} \rightarrow ^4I_{15/2}$ luminescence band shows multiple sublevels, whose relative individual contributions to the overall emission depend on the temperature due to the different population of the two sublevels E_1 and E_2 . By normalizing the spectra to the brightest peak ($E_1 \rightarrow (Z_7 + Z_8)$), one can observe that all E_2 -originating peaks increase with temperature (Fig. S1).

Note that some of the lines - in addition to temperature-induced broadening - experience minor spectral shifts of up to 5 cm^{-1} when going from cryogenic to ambient temperatures, as also reported in other works.^{S1} Furthermore, certain transitions originating from E_1 (e.g., $E_1 \rightarrow Z_6$) do not follow the same temperature dependence as the brightest peak, likely caused by a temperature dependence of the radiative decay rate. We attribute both of these changes to the lattice expansion of the surrounding yttria, since the crystal fields impact the resulting Stark wavefunctions.^{S2}

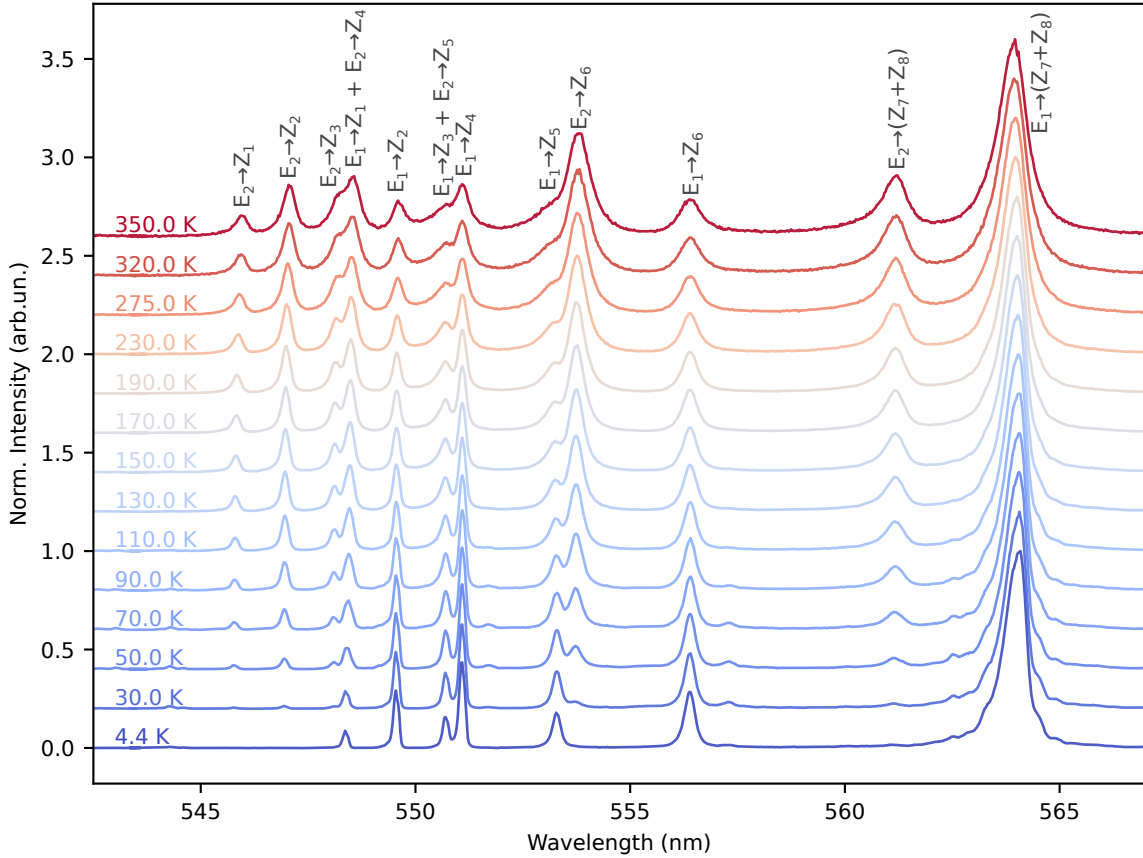


Figure S1: Normalized spectra of the $^4S_{3/2} \rightarrow ^4I_{15/2}$ luminescence band for various temperatures between 4.4 K and 350.0 K (offset for clarity). The assignments follow the empirical notation as detailed in the main text.

S2 Integrated intensity

Conventional ratiometric luminescence thermometry relies on the integrated intensities of the two manifold transitions ${}^2\text{H}_{11/2} \rightarrow {}^4\text{I}_{15/2}$ and ${}^4\text{S}_{3/2} \rightarrow {}^4\text{I}_{15/2}$. Fig. S2 shows their temperature-dependent count rates. As expected, the ${}^2\text{H}_{11/2}$ manifold has a negligible contribution to the emission spectra below 200 K, limiting its usefulness in cryogenic thermometry.

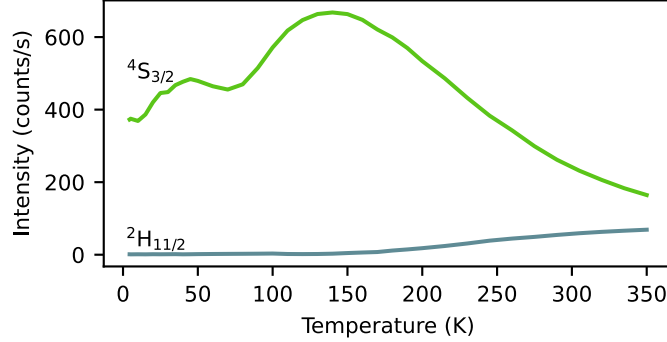


Figure S2: Integrated intensity of the ${}^2\text{H}_{11/2} \rightarrow {}^4\text{I}_{15/2}$ and ${}^4\text{S}_{3/2} \rightarrow {}^4\text{I}_{15/2}$ luminescence bands. For each temperature, the spectrum was integrated over 515 nm – 542 nm for the former and 542 nm – 580 nm for the latter.

S3 Voigt profile fitting

To accurately extract intensity ratios from partially overlapping Stark lines, simple spectral integration is insufficient due to finite linewidths and overlap from neighboring transitions. These linewidths arise from both homogeneous and inhomogeneous broadening: the former leads to Lorentzian line shapes, while the latter yields Gaussian components. Accordingly, we fit the emission lines with Voigt profiles, defined as the convolution:

$$V(x) = A_0 \int_{-\infty}^{\infty} G(x'; \sigma) L(x - x'; \gamma) dx', \quad (\text{S1})$$

where $G(x; \sigma) = \frac{1}{\sigma\sqrt{2\pi}} \exp\left(-\frac{(x-x_0)^2}{2\sigma^2}\right)$ is the Gaussian component and $L(x; \gamma) = \frac{\gamma/\pi}{(x-x_0)^2 + \gamma^2}$ is the Lorentzian. A_0 , x_0 , σ and γ are the fitting parameters.

Fig. S3 shows the spectrum at 350 K with overlaid Voigt fits for each resolvable transition; the two unfitted peaks (marked with an asterisk) contain overlapping contributions from at least three

levels, and were therefore excluded from the discussions due to a higher uncertainty in their fit.

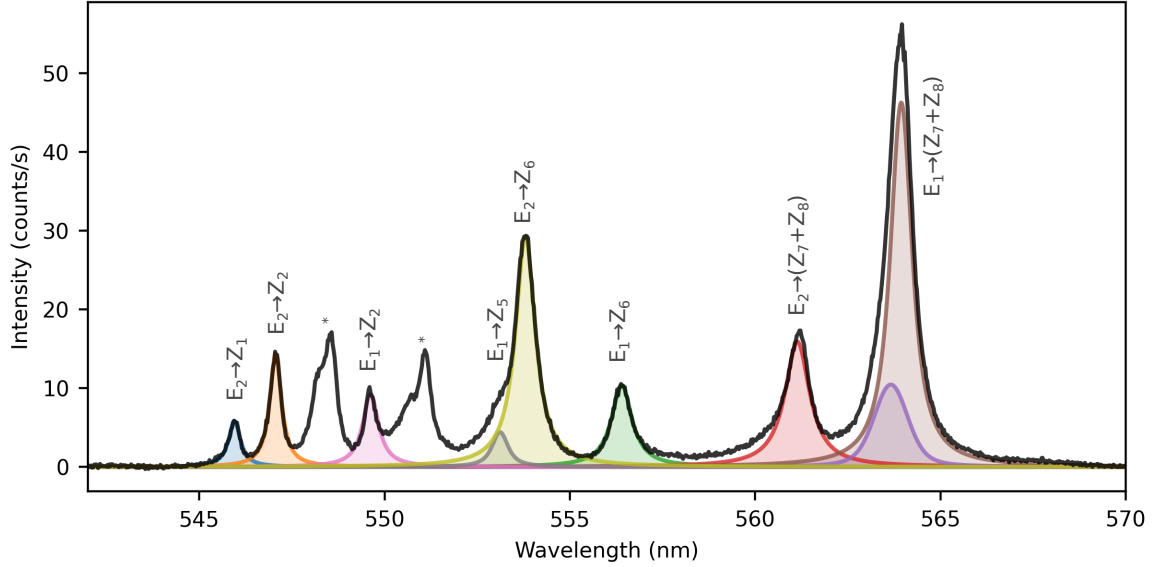


Figure S3: Emission spectrum of the $4S_{3/2} \rightarrow 4I_{15/2}$ band at 350 K, with overlaid fitted Voigt profiles. Peaks used in the analysis are labeled; the ones marked with an asterisk (*) are excluded.

S4 Sample characterization

The synthesized yttria nanoparticles doped with Yb^{3+} / Er^{3+} were characterized via X-ray diffraction (XRD). Measurements were conducted on a Siemens Bruker D5005 diffractometer operating with $CuK\alpha$ radiation ($\lambda = 1.5418 \text{ \AA}$) and equipped with a graphite monochromator. The diffractogram was recorded with a step of $0.02^\circ \text{ s}^{-1}$ in the 2θ range of 10° s^{-1} to 90° s^{-1} (Fig. S4a). The pattern shows good agreement with the reference spectrum for undoped cubic-phase yttria, confirming that the synthesized material retains a predominantly cubic crystalline structure.

Their morphology was examined under a JEOL JEM-100CX II Transmission Electron Microscope (TEM) operating at 100 kV (Fig. S4b). Ethanol was used to disperse the particles, allowing to measure their sizes. Average extracted diameters were $80 \pm 10 \text{ nm}$.

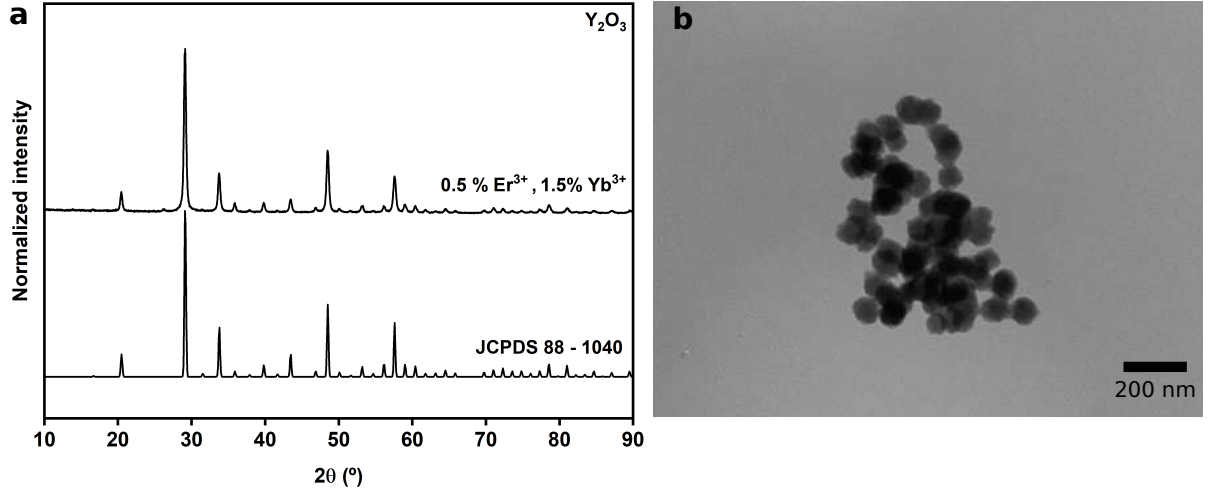


Figure S4: **a**, X-ray diffractogram of the Y_2O_3 : Yb^{3+} / Er^{3+} nanoparticles used in the experiments, with the corresponding reference spectrum for pure Y_2O_3 in its cubic phase (JCPDS 88-1040). **b**, TEM image showing particle morphology.

S5 Experimental setup

To characterize the sample at cryogenic temperatures, it was mounted in a liquid helium cryostat. Illumination was performed in reflection geometry (Fig. S5), using a tunable Ti:Sapphire laser emitting 140 fs pulses at a central wavelength of 980 nm.

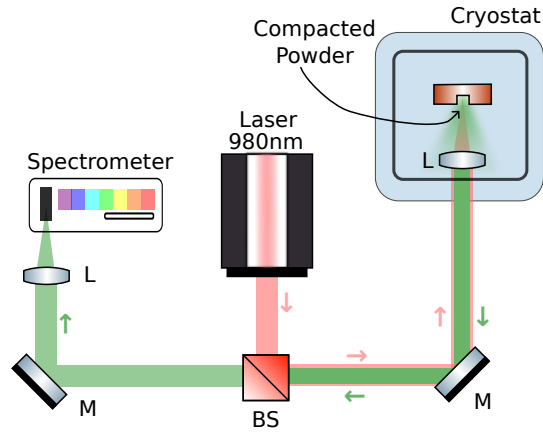


Figure S5: Schematic of the experimental setup for thermometric measurements. L: lens, M: mirror, BS: beam splitter.

References

- (S1) Dodson, A.; Wu, H.; Rai, A.; Apte, S.; O'Hara, A.; Lawrie, B.; Wang, Y.; Ueda, A.; Krzyżanowska, H.; Titze, M. *et al.* Phonon-mediated temperature dependence of Er^{3+} optical transitions in Er_2O_3 . *Communications Physics* **2024**, *7*.
- (S2) Ćirić, A.; Stojadinović, S.; Dramićanin, M. D. Temperature and concentration dependent Judd-Ofelt analysis of $\text{Y}_2\text{O}_3:\text{Eu}^{3+}$ and $\text{YVO}_4:\text{Eu}^{3+}$. *Physica B: Condensed Matter* **2020**, *579*, 411891.